Journal of Power Sources 666 (2026) 239065

Contents lists available at ScienceDirect

Journal of Power Sources

journal homepage: www.elsevier.com/locate/jpowsour

High-rate performance solid-state lithium batteries achieved by infiltrating a single-layer LLZO scaffold

Muhammad Zubair [a,b,*], Ruijie Ye [a], Xiaochen Liu [a], Kaouther Touidjine [a], Pradhyun Veerapanaicker Soundaraj [a], Martin Finsterbusch [a], Frank Tietz [a], Dina Fattakhova-Rohlfing [a,c], Olivier Guillon [a,d]

[a] Forschungszentrum Jülich GmbH, Institute of Energy Materials and Devices, Materials Synthesis and Processing (IMD-2), 52425, Jülich, Germany
[b] Batteries from Sustainable Materials, Just Transition Center, Martin Luther University Halle-Wittenberg, 06120, Halle, Germany
[c] University of Duisburg-Essen, Faculty of Engineering and Center for Nanointegration Duisburg-Essen (CENIDE), Lotharstraße 1, 47057, Duisburg, Germany
[d] Jülich-Aachen Research Alliance: JARA-Energy, 52425, Jülich, Germany

HIGHLIGHTS

- Single-layer LLZO ($Li_{6.45}Al_{0.05}La_3Zr_{1.6}Ta_{0.4}O_{12}$) scaffold is prepared by tape casting.
- Lithium metal was infiltrated into the single-layer scaffold's interconnected pores.
- A solid garnet-polymer separator is fabricated within unified framework.
- Solid-state full cell with $LiFePO_4$ exhibits capacity 106.7 (2C) and 76.7 mAh g^{-1} (5C).

GRAPHICAL ABSTRACT

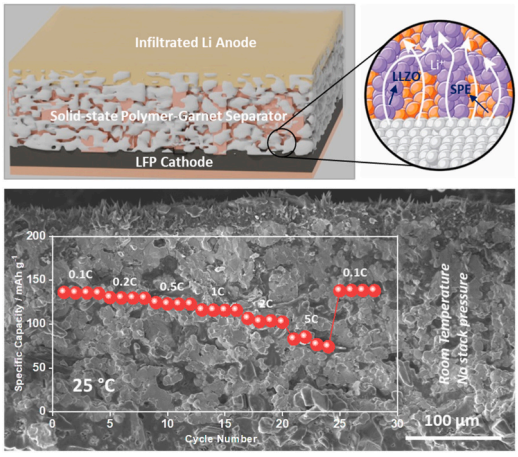

ARTICLE INFO

Keywords:
LLZO scaffold
Tape-casting
Infiltration
Composite solid-state electrolyte
Solid-state Li batteries

ABSTRACT

Ceramic-based lithium metal batteries widespread application is limited by the persistent difficulty in achieving stable performance under high c-rate conditions. Herein, we designed flat, thin (~200 µm) $Li_{6.45}Al_{0.05}La_3Zr_{1.6}Ta_{0.4}O_{12}$ single-layer 3D porous scaffolds by the tape-casting technique. Leveraging a meticulously engineered single-layer scaffold, lithium metal is uniformly infiltrated to an average thickness of 35 µm, ensuring seamless interfacial contact. Concurrently, a solid polymer electrolyte is integrated, facilitating the formation of a robust composite solid polymer-garnet separator with a precise thickness of 165 µm, all within a unified structural framework. The integrated single-framework not only reinforces structural and interfacial stability of the

* Corresponding author. Forschungszentrum Jülich GmbH, Institute of Energy Materials and Devices, Materials Synthesis and Processing (IMD-2), 52425, Jülich, Germany.
E-mail address: muhammad.zubair@physik.uni-halle.de (M. Zubair).

https://doi.org/10.1016/j.jpowsour.2025.239065
Received 2 October 2025; Received in revised form 23 November 2025; Accepted 6 December 2025
Available online 17 December 2025

metallic anode but also facilitates rapid Li^+ transport, markedly enhancing ionic conductivity. This synergistic effect enables exceptionally high-rate performance, paving the way for more efficient and reliable electrochemical applications. Full cells with lithium iron phosphate cathode and the Li-infiltrated single-layer ceramic/polymer electrolyte cycled at record current rates of 2C and 5C at room temperature and achieved 100 % capacity retention for 30 cycles at 0.1C. The discharge specific capacities at 2C and 5C are 106.4 and 76.7 mAh g^{-1}, respectively. This innovative single-layer framework is designed to enable high-current-density, room-temperature solid-state lithium-metal batteries while eliminating the need for stacking pressure.

1. Introduction

Over the past decade, the pursuit of safer and higher energy density storage has driven significant interest in solid-state lithium-metal batteries (SSLB). Among solid electrolytes, garnet-type Li_{7-x} $La_3Zr_{2-y}O_{12}$ (LLZO, with x = Al, and y = Ta) manifests a promising solid electrolyte and the only solid electrolyte with wide electrochemical stability window (0–9 V vs. Li) [1–3] enabling Li usage and also providing relatively high ionic conductivity (10^{-4}–10^{-3} S cm^{-1}) at room temperature [4,5]. However, realizing its potential in practical full-cell configurations remains challenging.

A key limitation lies in processing LLZO into thin, mechanically robust separators that can sustain full-cell integration. While the high stiffness of LLZO offers effective suppression of lithium dendrite growth which is a critical problem in conventional Li-ion batteries [6,7], it hinders intimate contact with both the cathode and lithium metal during cycling. Conventionally, in most of the published papers, LLZO has been used in the form of thick sintered pellets [8], often co-sintered with cathode materials such as $LiCoO_2$ to maintain interface contact [9,10]. These cells suffer from low energy density due to the pellet thickness, degradation during high temperature co-sintering, interface stability, and severe capacity fading during early cycles, largely driven by mechanical mismatch and loss of interfacial contact during volume changes upon cycling [11–13].

To overcome energy density limitations, tape casting has been used as a promising route for fabricating thin LLZO films given its maturity, scalability and cost-effectiveness [14–16]. But to unlock the full potential of LLZO, the design and the architecture of full cells must be figured out. More recently, the development of porous LLZO scaffolds has gained attraction, as they allow infiltration of cathode active materials (CAM) and lithium (Li) metal, enhancing interfacial contact areas which improves electrochemical exchange rate, thus improving capacity and energy density. Notably, Rupp et al. [17] and Wachsman et al. [18] have demonstrated full-cell architectures based on multilayer LLZO separators, typically involving a dense core layer flanked by porous layers for material infiltration. However, these approaches often rely on costly and complex lithium infiltration techniques such as physical or chemical vapor deposition (PVD/CVD) [19,20]), or pre-coating steps using materials like alumina [21], which increase fabrication complexity and hinder scalability. It is worth noting, that maintaining stable interfaces during cycling is a determining factor to achieve stable LLZO solid-state battery cycling. Delamination and contact loss at both cathode and lithium interfaces are common failure modes [22–24]. A practical method to mitigate the interfacial problems during cycling is incorporating a chemically compatible solid polymer electrolyte (SPE) into the LLZO porous network. It offers dual benefits: 1) stabilizes interfaces through its elastic mechanical properties; 2) maintains Li^+ transport junction at high cycling rates when volume change and contact loss becomes prominent [25,26].

To utilize the advantages of the described approaches to infiltration, here a meticulously engineered porous single-layer scaffold is uniformly infiltrated with lithium metal to a limited thickness, ensuring seamless interfacial contact. Concurrently, a SPE is integrated, facilitating the formation of a robust composite solid polymer/garnet separator, all within a unified structural framework. The Li infiltration can be achieved through simple melting process, while SPE formation can be achieved through in-situ polymerization technique to wet the LLZO porous surface before full-cell performance. In this work, we demonstrate the feasibility to produce a flat, porous free-standing single-layer of LLZO fabricated via tape casting, co-infiltrated with a Li anode and solid polymer electrolyte (schematic Fig. 1a–d). This architecture enables direct infiltration of Li metal (~35 μm) and the integrated solid-polymer phase. A single unified porous framework improves ionic conductivity and mechanical compliance, allowing the cell to operate at high current rates. Notably, solid-state full cells against $LiFePO_4$ cathode assembled using this design successfully cycled at 0.1C and eventually can reach 2C and 5C at room temperature, achieving, for the first time, such high C-rates in a single-layer LLZO-based solid-state architecture without external pressure.

2. Experimental

2.1. Preparation of free-standing single-layer LLZO scaffold

The LLZO powder with the composition $Li_{6.45}Al_{0.05}La_3Zr_{1.6}Ta_{0.4}O_{12}$ containing 10 wt% Li excess was synthesized via solid-state reaction as described previously [14]. A water-based tape casting method [15] was applied here to prepare the free-standing LLZO single-layers. For a typical preparation of the suspension, 0.45 g methylcellulose (4000 cP (cP), Alfa Aesar), 1.8 g polyethylene glycol (Mw 400, Merck), and 1.8 g glycerol (99 %, Merck) were dissolved in deionized water by magnetic stirring to form a polymer solution. Afterwards, 4.5 g poly(methyl methacrylate) powder (PMMA 40 μm, EPRUI Biotech Co. Ltd) with the uniform particle size of 40 μm were added into the previous polymer solution, and well mixed by a planetary mixer at 1500 rpm for 2 min to form a PMMA suspension. Subsequently, 10 g LLZO powder were poured into this suspension, and well mixed for another 3 min at 1500 rpm to form the slurry for tape casting. The prepared slurry was cast on a Mylar foil using a moving doctor blade with a gap height of 600 μm. The green tapes were manually peeled off after drying overnight in ambient atmosphere. Two layers of the green tapes were laminated at 80 °C with a pressure of 30 MPa for 2 min, then punched out into discs with a diameter of 10 mm. The discs were placed on MgO plates with LLZO coatings inside a closed alumina crucible. The crucible was heated up in air at a heating rate of 2 °C min^{-1} to 750 °C with 1 h dwell time for burning out the organic substances and subsequently at a heating rate of 5 °C min^{-1} to 1175 °C with 6 h dwell time for sintering. After free cooling to room temperature, the samples were transferred into an alumina boat inside a tube furnace, and annealed with flowing Ar at 800 °C with 1 h dwell time to remove Li_2CO_3 impurities. After cooling, the free-standing porous LLZO single-layer scaffolds were obtained and stored in an Ar-filled glovebox. The diameter of the annealed LLZO scaffold (inset b in Fig. 2a) was reduced to 8 mm, indicating volume contraction due to the successful sintering of the ceramic scaffold. Despite the volume change, the LLZO scaffold still possesses a high porosity content, as shown in Fig. 2b and c, the top view and polished cross-sectional SEM images of the LLZO scaffold, respectively. The porosity of the LLZO scaffold was determined by statistical analysis of ≥5 SEM cross-sections to report (average porosity ± standard deviation). Interestingly, the average porosity ± standard deviation was 38.46 ± 2.6 %. The bulk density measurement was calculated, and the porosity was found to be 37.76 %, close to 38.46 % (the calculation

dataset and Fig. S1 and S2 is in the supplementary information (SI)). The thickness of the obtained single-layer porous LLZO scaffold (SL) was ~200 μm and the interconnected average pore size was around ~25–40 μm (Fig. 2c and d).

2.2. Lithium and polymer solid electrolyte infiltration

The Li infiltration process was started once the SL was transferred into the Ar glovebox to keep the SL surface as clean as possible. First, a thin Au sputtered interlayer (~20 nm) was applied to the scaffold by using a sputter coater (Cressington 108cuto coater) for a sputtering time of 20 s with a distance of 6.5 cm between the sample. The sputtered current was 20 mA under an Ar pressure of ~0.02 mbar [14,45]. Freshly rolled Li metal foil was melted on a hot plate using a nickel disk as a base, and the SL was placed on top of it. The sample was then heated to 300 °C for 15 min while cooling for 30 min to ensure Li infiltration into the pores with good electrical and mechanical contact. SEM images showed that the average infiltration depth of Li into the scaffold was ~35 μm (Fig. 3b). Hereafter, the Li-infiltrated SL is named as Li@SL (Fig. 1b).

The preparation of the SPE precursor started with mixing 2.5 g 1,3,5-trioxane (TXE) and the desired amount of butanedinitrile (BN) in the mass ratio of 5:3. Then the mixture was melted at the elevated temperature of 80 °C for 10 min to obtain a eutectic solution. Subsequently, 0.365 g lithium difluoro(oxalato)borate (LiDFOB) was added to the eutectic solution and stirred for 1 h at 50 °C in a sealed glass bottle to obtain a transparent precursor. Now, 30 μl of the SPE precursor solution was dropped onto the other side of Li@SL and dried in the glove box at 80 °C for in-situ polymerization. During this process, LiDFOB initiated the in-situ polymerization of eutectic solution to generate the SPE within the scaffold. In the following, the Li@SL infiltrated with SPE is abbreviated as Li@SL@SPE. One SL was completely infiltrated with SPE (SL@SPE) to compare the Li^+ conductivity of the SL and SPE-infiltrated SL.

To test the electrochemical performance of the Li@SL@SPE in a full cell, $LiFePO_4$ (LFP, MSE supplies) cathodes were prepared. For the cathode slurry, LFP, carbon black and polyvinylidene fluoride (PVDF) were homogenously dissolved in N-methyl-2-pyrrolidone (NMP) solvent at a weight ratio of 80:10:10. Then the slurry was cast onto aluminum foil using doctor blade and dried in a vacuum oven at 80 °C for 12 h. The cathodes were punched out in slices with a diameter of 8 mm, weighed and dried in an oven at 80 °C for 8 h. The LFP loading was ~3 mg cm^{-2}. The full cells with Li@SL@SPE were assembled with LFP cathode in an Ar glovebox with H_2O and O_2 levels below 0.5 ppm. The cell was left at 80 °C overnight and then naturally cooled to room temperature to obtain good interfacial contact between Li@SL@SPE and the cathode.

2.3. Characterizations

The crystal structure of samples was investigated by X-ray diffraction (XRD; Cu K_α radiation, Bruker D4 Endeavor voltage 40 kV). To examine the morphology of the scaffolds, the pristine SL samples were fractured and embedded in epoxy resin (EpoFix) and mirror polished, whereas the infiltrated samples were fractured only. Scanning electron microscopy (SEM, Carl Zeiss Microscopy, Zeiss EVO 15) joint with energy-dispersive X-ray spectroscopy (EDS, Oxford Instruments plc, Abingdon, UK) was used to study morphology and elemental composition. Raman spectra (Renishaw INVIA Raman Microscope, equipped with a solid-state excitation laser (532 nm) and a 2400 lines/mm grating) were measured at a laser power of 2.5 mW and the exposure time was set at 1 s per spectrum.

2.4. Electrochemical measurements

Impedance spectroscopy was used to determine the Li^+ conductivity using Au as blocking electrodes for both SL, and SL@SPE. Impedance measurements were performed at 25 °C using a Bio-Logic work station (VMP-300 multi-potentiostat) with the frequency range from 7 MHz to 1 Hz and an electric field perturbation of 10 mV mm^{-1}. All measurements were fitted to extract resistance (R) using the software RelaxIs 3 (rhd Instruments GmbH & Co. KG) for fitting and Distribution of Relaxation Times (DRT) analysis. The Li^+ conductivities were obtained using the formula

$$\sigma_m = \frac{1}{R}\frac{L}{A_{geo}} \quad \text{Equation 1}$$

where L is the sample thickness, and A_{geo} is the area. The Bruggeman symmetric medium theory was used to consider the impact of porosity on the total resistance of the porous LLZO scaffold, thereby calculating

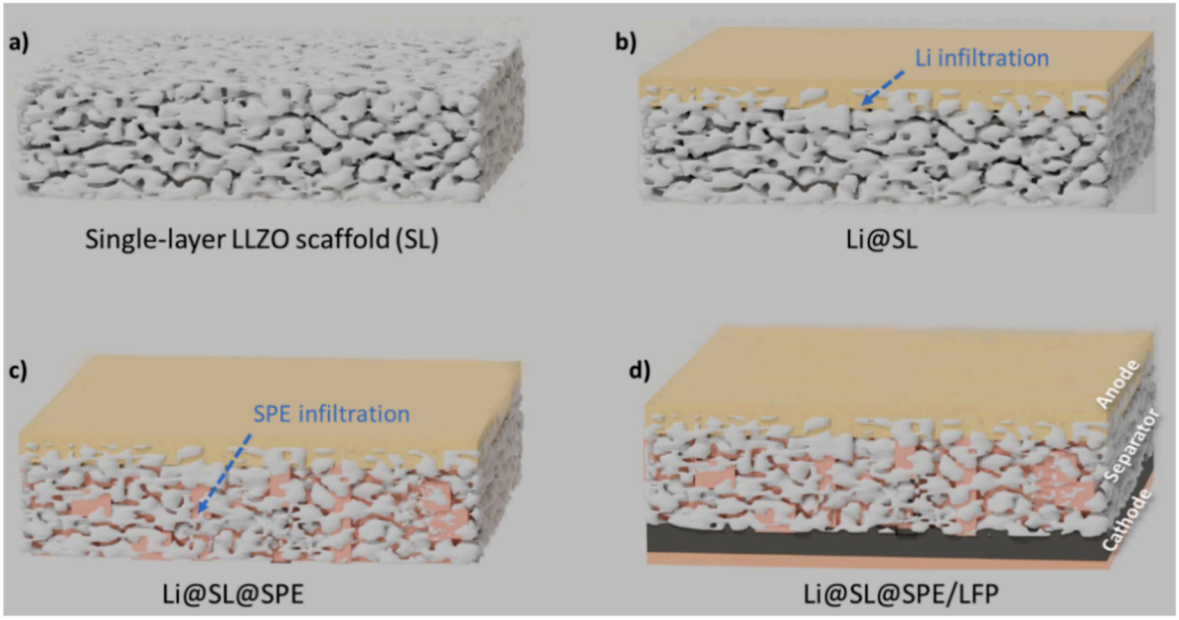

Fig. 1. Schematic illustration of a full cell preparation a) SL, b) Li-infiltrated SL (Li@SL), c) Li@SL infiltrated with SPE (Li@SL@SPE), d) SSLB consist of Li@SL@SPE/LFP

the actual ionic conductivity of the porous LLZO [27,28]. This theory assumes the porosity as a low-conductivity phase, relates the measured conductivity (σ_m) to the geometric dimensions of the scaffold (thickness and area), adjusts for the porosity (σ_h) with the volume fraction of porosity (f) using the equation

$$\sigma_m = \sigma_h\,(1 - 3/2\,f) \qquad \text{Equation 2}$$

The critical current density (CCD) of Li@SL@SPE samples were assessed by assembling Li symmetrical cells and tested by rate cycling with increasing steps of 14 μA cm^{-2} until 98 μA cm^{-2} at an initial current density of 14 μA cm^{-2} keeping constant the plating and stripping time at 1 h. Later, the CCD test was extended to 196 and 392 μA cm^{-2}. All electrochemical performance tests on full cells were performed using a Bio-Logic program control system with a planned charge/discharge current density maintaining at 1C = 170 mAh g^{-1} for the LFP cathode at room temperature (25 °C). All electrochemical cells were assembled in Swagelok cells.

3. Results and discussion

According to XRD, the crystal structure of the single-layer porous LLZO scaffold is a cubic garnet-type single phase without any other impurities corresponding to cubic LLZO [29] (Fig. 2a). The vertical red line is a cubic LLZO structure, identified by ICDD JCPDS card number 99-000-0032. The inset, Fig. 2b, shows a digital image of a SL with a diameter of approximately 8 mm. Typical SEM images of the microstructure of SL are shown in Fig. 2c and d. The images show uniformly distributed and well-interconnected pores on the surface (Fig. 2c) and through the entire thickness of the scaffold (Fig. 2d). The LLZO scaffold forms a 3D conductive framework with micron-sized porous channels. Such open pores on surface and in the entire bulk are beneficial for the infiltration of Li metal and the in-situ polymerization of polymers. The EDS results confirmed the uniform distribution of all constituent elements of the garnet including Al and Ta (Fig. S3).

Solid-state Li-metal battery assembly starts with Li metal infiltration into the single-layer. Fig. 1a–d gives a schematic sequence of the battery assembly. In a typical procedure, the SL was placed on molten Li and maintained at 300 °C for 15 min to control the infiltration process to the desired level by capillary force. It is important to note that the cubic garnet-type compound exhibits poor Li wettability and hinders infiltration (Fig. S4). The applied Au layer on the surface prevents poor wetting [9,30,31]. After infiltration, the SEM image of the single-layer cross-section clearly shows Li embedded in the pores of the upper layer of SL (Fig. 3a and b). The close-up view shows a strong Li-LLZO interface where Li fills the dashed rectangle of the LLZO particles. Fig. 3b shows that the average depth of the infiltrated Li within the SL is 35 μm. The yellow dashed line in the wider view shows the control limit of Li infiltration in the SL (Fig. S5). The remaining porous section of Li@SL is used to insert the solid-state polymer electrolyte (Fig. 3c).

Prior to infiltrating SPE into Li@SL, an SL was first completely infiltrated with SPE to test its compatibility and ionic conductivity. Raman spectra of the sample SL@SPE can be seen in Fig. 4a. The given spectrum shows the presence of LLZO as the dominant phase, which means that this phase remains intact during all SPE infiltration steps for in-situ polymerization. Some additional peaks at 156 cm^{-1}, 194 cm^{-1}, and 1090 cm^{-1} in the Raman spectrum are characteristic of Li_2CO_3 at the surface [26], likely formed during the Raman measurement since it is conducted in ambient condition where some CO_2 uptake is expected to occur. Moreover, the main peaks of SL@SPE at 539 cm^{-1}, 673 cm^{-1}, 917 cm^{-1}, 933 cm^{-1}, 973 cm^{-1} and 1033 cm^{-1} were observed, indicating the formation of SPE within the SL scaffold after in-situ polymerization [32–34] while the peaks at 624 cm^{-1}, 715 cm^{-1}, 873 cm^{-1} are related to LiDFOB [35–37]. Impedance spectroscopy was employed to compare the ionic conductivity (σ_{RT}) of SL and SL@SPE at 25 °C (Fig. 4b). The Nyquist plot shows two semicircle for SL@SPE and only semicircle for SL, which contains the bulk and grain-boundary resistances used to calculate σ_{RT}. By fitting the impedance data (Table S1 and Fig. S6), the total resistance of the sample is 311.2 Ω for SL and 70.3

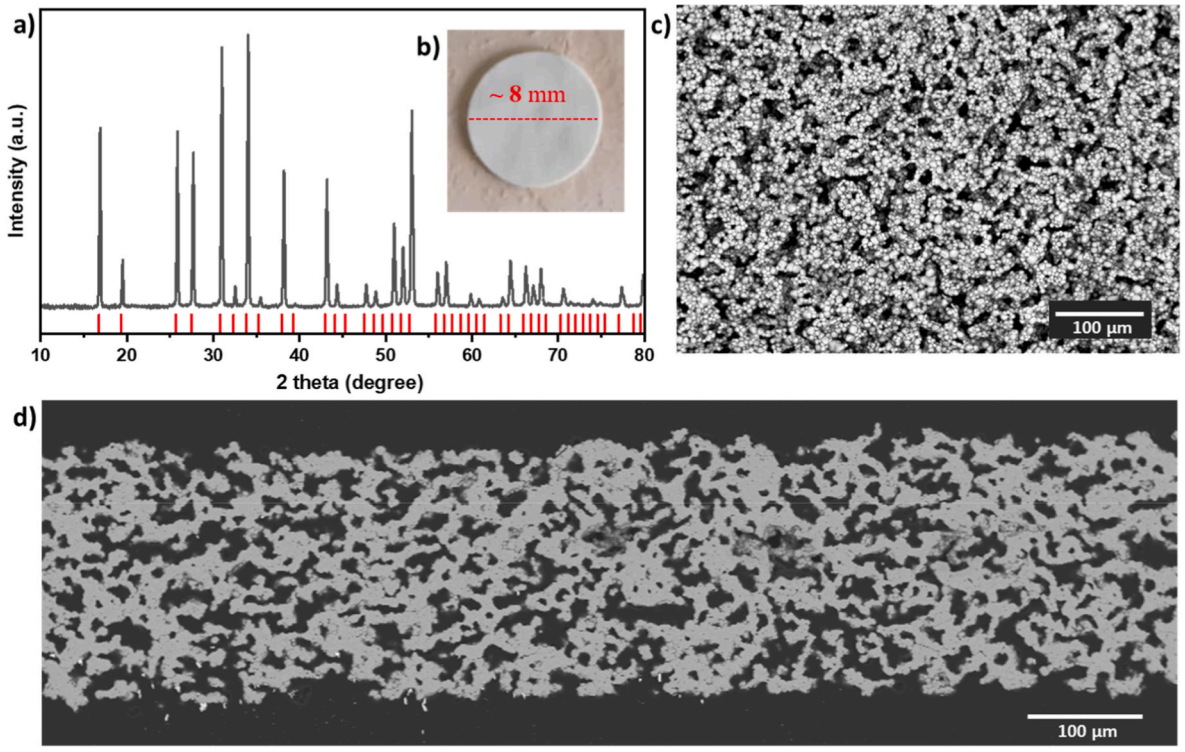

Fig. 2. a) XRD pattern of SL, the vertical red line is a cubic LLZO structure, identified by ICDD JCPDS card number 99-000-0032; b) digital picture of SL, c) SEM image of the top view of SL exhibiting high open porosity, which is beneficial for infiltration, d) cross-sectional view of SL showing high porosity and interconnected porous structures. (For interpretation of the references to colour in this figure legend, the reader is referred to the Web version of this article.)

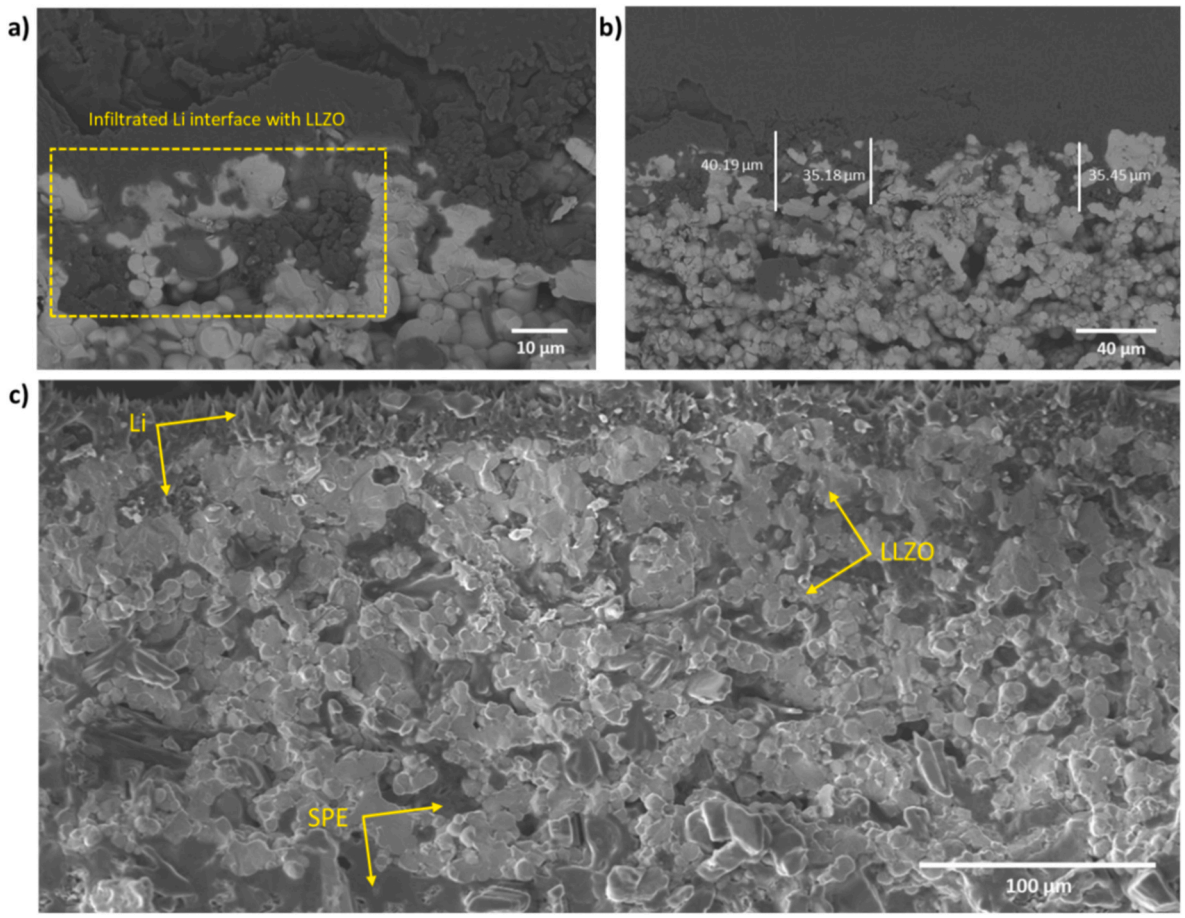

Fig. 3. SEM images of Li-infiltrated SL cross-sectional fractures: a) closer view shows intimate Li interface with LLZO, b) wider view to show the average depth of infiltrated Li in SL (~35 µm), c) secondary electrons SEM image of Li@SL@SPE showing successful infiltration of Li and SPE in a single scaffold structure.

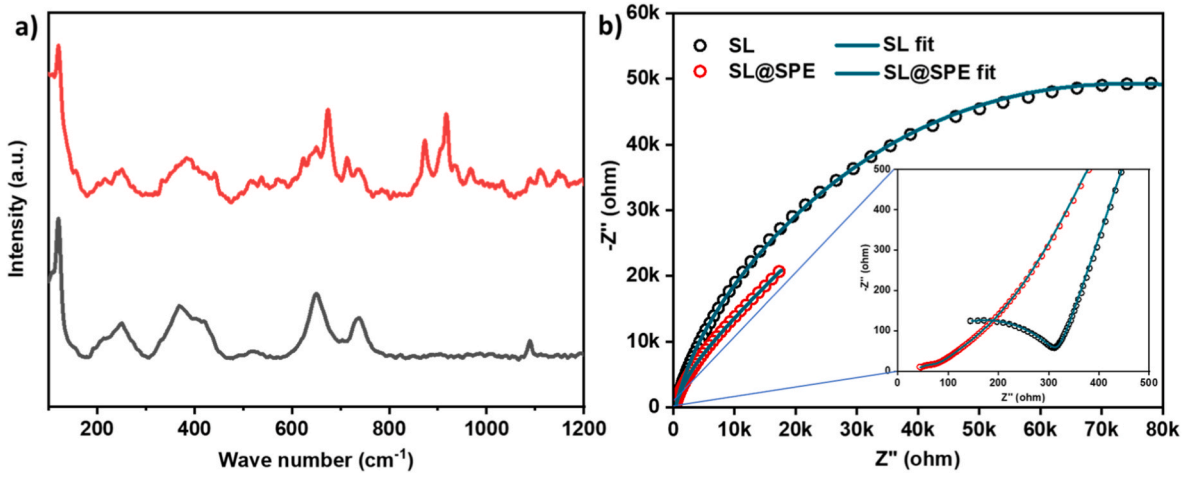

Fig. 4. a) Comparison of Raman spectra of SL (bottom) and SL@SPE (top), b) impedance spectra of the SL and SL@SPE separators recorded at 25 °C.

Ω for SL@SPE after polymer infiltration. Thus, the calculated σ_{RT} of the SL@SPE is 0.55 mS cm^{-1}, which is much higher than 0.28 mS cm^{-1} of SL. We used Equation (2) to calculate σ_{RT} of SL. The first semicircle of SL@SPE is actually the grain boundary contribution, while the bulk contribution is shown as a series resistor in the Nyquist plot. The contribution from LLZO/polymer interface, merged in the large resistance of pores, is hard to separate. Therefore, the SPE indeed reduced (or filled) the pores, giving rise to a reduction of total resistance. These values are consistent with those reported in the literature [28]. The high ionic conductivity of SL@SPE would increase the Li^+ transport capability and low-temperature dependence. DRT analysis was performed on the SL and SL@SPE, where τ_1 represents grain boundaries, τ_2 represents pores and the SL/SPE interface, and τ_3 represents the charge transfer process at the SE/Au interface (high resistance might be due to the blockage effect) (Fig. S7). A new peak was found in SL@SPE at 10^{-6}-10^{-5} s (marked as * in Fig. S7), which may correspond to the

SL/SPE interface. Therefore, EIS measurements, and appearance of additional peak in DRT profiles, which both points to more effective Li^+ transport pathways through the new formed LLZO/SPE interfacial contact. In the following, the SPE was infiltrated into the Li@SL samples to serve as a composite solid electrolyte separator, as shown in Fig. 3c. The image proves the effective infiltration of Li, the good interface between Li and LLZO, and the homogeneous composite of SPE and LLZO embedded in a single framework.

Beside the good conductivity, the dendrite suppression ability is an important parameter to qualify the SL@SPE as a good electrolyte. Thus, to evaluate this, Li symmetric cells were assembled with Li@SL@SPE samples and tested. Capacitive critical current density measurement (CCD), shown in Fig. S8, did not result in short-circuiting the Li@SL@SPE samples even at a current density of 392 μA cm^{-2}, resulting in a total of ≥100 h (105 h) of stable operation and the symmetric cells can still recover to stable cycling after a short period of slight polarization. Thus, these measurements confirm that the interface between the porous ceramic channels and the SPE filler improves the conductivity enabling the rapid Li^+ transport across the interface, while the composite scaffold can resist Li dendrite formation. Therefore, the SL@SPE architecture possesses the necessary parameters including stability against Li metal and good ionic conductivity to be used in a full cell

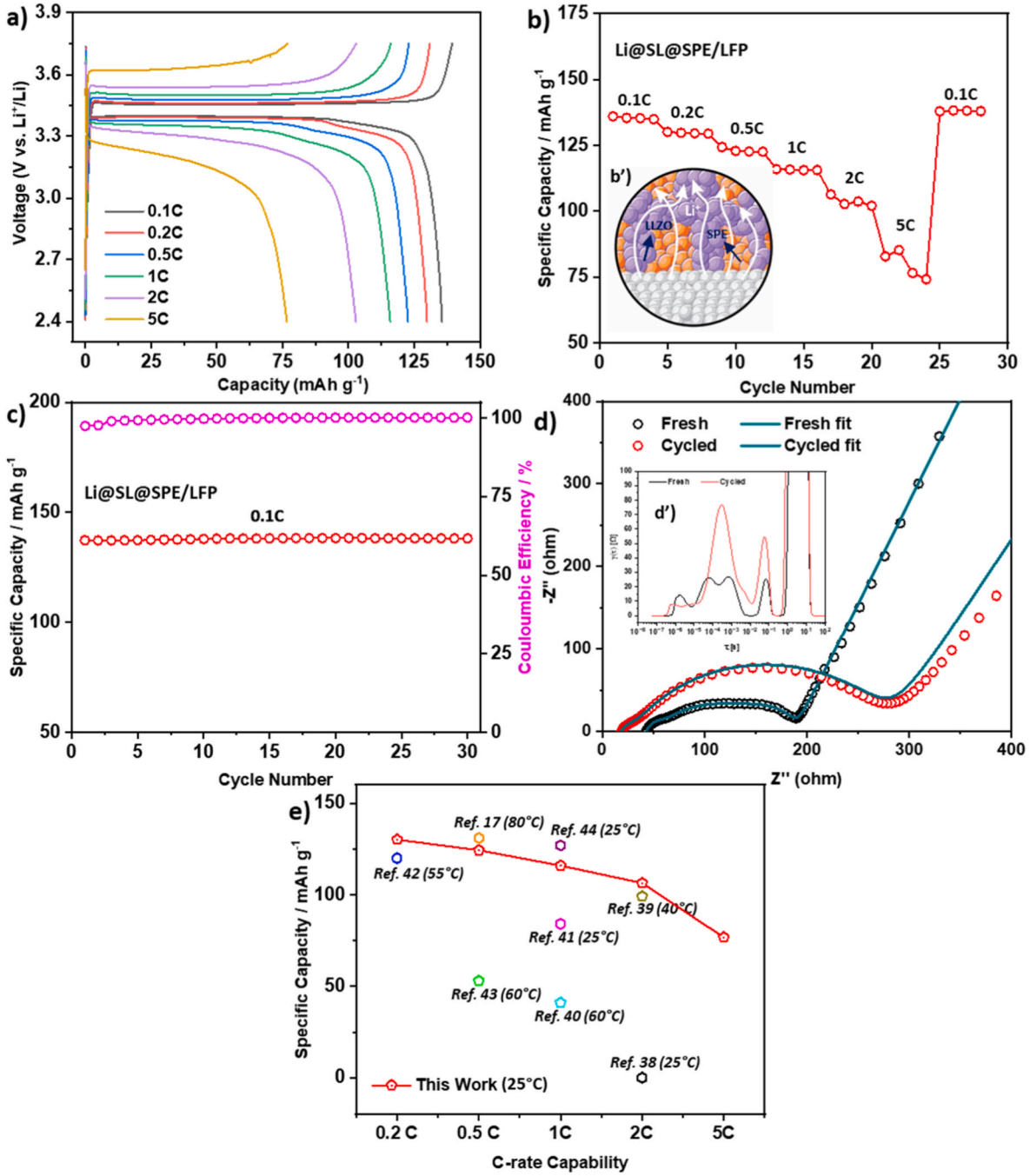

Fig. 5. a) Charge/discharge profiles of full-cell Li@SL@SPE/LFP at different C-rates 0.1C, 0.2C, 0.5C, 1C, 2C and 5C between 2.4 and 3.75 V, b) the corresponding rate performance graph, inset b') is the schematic illustration of parallel ion-transport pathways through LLZO grains and SPE channels, c) cycling performance of Li@SL@SPE/LFP at 0.1C between 2.4 and 3.75 V, d) EIS spectra of fresh and cycled cell and inset d') is the following DRT analysis, e) comparison of discharge capacity of Li@SL@SPE/LFP with different garnet-based porous scaffolds in LFP-based SSLB.

configuration.

Solid-state full-cells with Li@SL@SPE were assembled in combination with lithium iron phosphate (LFP) cathodes in Swagelok cell configuration, as shown in schematic Fig. 1d.

The rate capability of the cell was evaluated at various charging and discharging rates ranging from 0.1 to 5C (Fig. 5a and b). First, the galvanostatic charge/discharge curves of the presented cell was compared at different rate conditions (1C = 170 mA g^{-1}) and in the voltage range 2.4–3.75 V at 25 °C. As shown in Fig. 5a, all C-rates show the typical charging curves of LFP. The specific discharge capacities at 0.1, 0.2, 0.5, 1, 2 and 5C are stable at 136.0, 130.1, 124.3, 116.0, 106.4 and 76.7 mAh g^{-1}, respectively (Fig. 5b). When the current density returned to 0.1C, the specific discharge capacity delivered 138.0 mAh g^{-1}. Nevertheless, to the best of our knowledge, the high C-rate performance and discharge capacity (i.e., 106.4 and 76.7 mAh g^{-1}) of the full cell based on LLZO scaffold at 2C and 5C are one of the first attempts to fabricate fast-charging SSLBs based on $LiFePO_4$ as cathode and Li anode at room temperature. Moreover, compared with other garnet-based SSLBs with $LiFePO_4$ cathode, (Fig. 5e and Table S3), the porous scaffold approach exhibits the highest discharge capacity at high C-rates and was the only system operating at 5C and 25 °C [17,38–44]. The good rate performance of the cell is primarily attributed to its 3D SPE-garnet composite structure. The polymer infiltrates into the interconnected LLZO scaffold, forming parallel and continuous ion-transport percolations: 1) rapid Li^+ conduction along the LLZO grains; 2) the flexible and closely fitted SPE channels effectively connect grain boundaries and fill pore spaces. This dual-network structure increases the overall percolation probability of Li^+ migration, resulting in an overall conductivity higher than either standalone phase. A schematic diagram (Fig. 5b, inset b') illustrates the parallel transport of Li^+ within the LLZO grains and the SPE-filled channels. It is also worth noting that the improved conductivity of SL@SPE is a key enabler for the cell to sustain high C-rates without complete failure. The fitted values indicate that both contributions favor high-rate cycling. These results are consistent with the enhanced effective percolation of the Li^+ transport pathway in the composite electrolyte. The polymer residual at the cathode/SPE could also sustain the contact with the cathode layer upon cycling where delamination often occurs in LLZO-based SSLBs. The results of the long-term cycling of the full cell at 0.1C and 25 °C are shown in Fig. 5c, where the capacity remains stable at 137 mAh g^{-1} for tens of cycles with a capacity retention rate of 100 %. This confirms that the good contact of the cell components including the Li and the cathode layer interface are well maintained. EIS spectra before and after cycling of full cells shown in Fig. 5d. The fitting results indicate that even after 30th cycle, the ceramic-polymer interface of the fresh and the cycled cell did not change significantly (Fig. S9, Table S2) and remains stable. This hypothesis is confirmed by SEM images of Li@SL@SPE after charge-discharge cycling of the full cell (Fig. S10). After cycling, the sample still exhibits good integrity, and the interfaces between Li metal, SPE, and LLZO scaffold are well connected with clear interface boundaries, with no obvious abnormalities even after tens of cycles. Although techniques such as Transmission electron microscopy (TEM) and X-ray photoelectron spectroscopy (XPS) could provide additional nanoscale details into interfacial evolution, the combination of stable overpotential behavior and the clean post-cycling morphology observed by SEM already confirms robust interface retention in our system. A more comprehensive nanoscale analysis using TEM/XPS will be pursued in future work to further expand these findings. To test the validity of framework at high voltage cathodes, the electrochemical stability window of the SPE was measured using linear sweep voltammetry (LSV) in a Li/SPE/SS configuration, as shown in Fig. S11. SPE exhibited an oxidative stability of >4 V. Such a high electrochemical window makes the Li@SL@SPE framework suitable for high-voltage cathodes [43, 51, 58]. The results prove that our approach using the in-situ polymerization to design 3D Li@SL@SPE can effectively enable the integration of a single LLZO layer to a full cell. The constructed polymer network inside the porous LLZO improves the interfaces to cathode and anode enabling stable cycling without cell failure. The Li@SL@SPE unit delivered good electrochemical performance with high and stable capacity that is mainly attributed to the stable interfaces with the electrodes.

4. Conclusion

In summary, we have designed a garnet-based SSLB featuring a distinctive single-layer 3D ion-conducting host and a thin composite separator within a unified framework. The free-standing porous membrane, produced through industrially feasible tape casting using $Li_{6.45}Al_{0.05}La_3Zr_{1.6}Ta_{0.4}O_{12}$, facilitates lithium infiltration into interconnected pores of approximately 35 μm. A composite solid polymer–garnet separator (165 μm) is formed in situ, effectively separating the lithium metal anode from the $LiFePO_4$ cathode. The resulting solid-state full cell exhibits outstanding high-rate capability at ambient temperature (up to 5 C, 76.7 mAh g^{-1}) and demonstrates remarkable cycling stability. This work underscores the promise of garnet-based ceramics for next-generation solid-state lithium batteries.

CRediT authorship contribution statement

Muhammad Zubair: Writing – original draft, Methodology, Investigation, Formal analysis, Data curation, Conceptualization. **Ruijie Ye:** Writing – review & editing, Methodology, Conceptualization. **Xiaochen Liu:** Validation, Methodology, Investigation. **Kaouther Touidjine:** Writing – review & editing, Investigation, Data curation. **Pradhyun Veerapanaicker Soundaraj:** Visualization, Methodology. **Martin Finsterbusch:** Writing – review & editing, Resources, Project administration, Funding acquisition, Conceptualization. **Frank Tietz:** Writing – review & editing, Supervision, Project administration, Funding acquisition, Formal analysis, Conceptualization. **Dina Fattakhova-Rohlfing:** Writing – review & editing, Resources, Project administration, Investigation, Funding acquisition, Conceptualization. **Olivier Guillon:** Visualization, Supervision, Project administration, Methodology, Investigation, Funding acquisition.

Declaration of competing interest

The authors declare that they have no known competing financial interests or personal relationships that could have appeared to influence the work reported in this paper.

Acknowledgements

Financial support by the German Federal Ministry of Research, Technology and Space (projects FestBatt 2-Oxid, grant number 13XP0434A, FestBatt 2-Hybrid, grant number 13XP0428A, NASS, grant number 13XP0490B) is gratefully acknowledged. The authors take responsibility for the content of this publication. K. T. acknowledges funding from the DESTINY European doctorate program in the frame of the European Union's Horizon2020 research and innovation program under the Marie Skłodowska-Curie Actions COFUND-grant agreement no. 945357.

Appendix A. Supplementary data

Supplementary data to this article can be found online at https://doi.org/10.1016/j.jpowsour.2025.239065.

Data availability

Data will be made available on request.

References

[1] J. Huang, C. Li, D. Jiang, J. Gao, L. Cheng, G. Li, H. Luo, Z.L. Xu, D.M. Shin, Y. Wang, Y. Lu, Solid-state electrolytes for lithium metal batteries: state-of-the-art and perspectives, Adv. Funct. Mater. 35 (1) (2025) 2411171.

[2] Y. Benabed, A. Vanacker, G. Foran, S. Rousselot, G. Hautier, M. Dollé, Solving the Li7La3Zr2O12 electrochemical stability window puzzle, Mater. Today Energy 35 (2023) 101320.

[3] Y. Zhu, X. He, Y. Mo, Origin of outstanding stability in the lithium solid electrolyte materials: insights from thermodynamic analyses based on first-principles calculations, ACS Appl. Mater. Interfaces 7 (42) (2015) 23685–23693.

[4] X. Li, F. Luo, N. Zhou, H. Adenusi, S. Fang, F. Wu, S. Passerini, Weakly solvating electrolytes for lithium and post-lithium rechargeable batteries: progress and outlook, Adv. Energy Mater. 15 (2025) 2501272.

[5] L. Ma, J. Zhao, M. Li, H. Su, Y. Li, Y. Liu, H. Liu, E. Zygadło-Monikowska, Y. Xu, Quasi-solid electrolytes with flexible branches and rigid skeletons for high-temperature Li metal batteries, ACS Appl. Mater. Interfaces 17 (12) (2025) 18206–18216.

[6] Y. Wang, Z. Chen, K. Jiang, Z. Shen, S. Passerini, M. Chen, Accelerating the development of LLZO in solid-state batteries toward commercialization: a comprehensive review, Small 20 (35) (2024) 2402035.

[7] C. Yildirim, F. Flatscher, S. Ganschow, A. Lassnig, C. Gammer, J. Todt, J. Keckes, D. Rettenwander, Understanding the origin of lithium dendrite branching in $Li_{6.5}La_3Zr_{1.5}Ta_{0.5}O_{12}$ solid-state electrolyte via microscopy measurements, Nat. Commun. 15 (1) (2024) 8207.

[8] J. Guo, C.K. Chan, Lithium dendrite propagation in Ta-Doped $Li_7La_3Zr_2O_{12}$ (LLZTO): Comparison of reactively sintered pyrochlore-to-garnet vs LLZTO by solid-state reaction and conventional sintering, ACS Appl. Mater. Interfaces 16 (4) (2024) 4519–4529.

[9] C. Roitzheim, Y.J. Sohn, L.Y. Kuo, G. Häuschen, M. Mann, D. Sebold, M. Finsterbusch, P. Kaghazchi, O. Guillon, D. Fattakhova-Rohlfing, All-solid-state Li batteries with NCM-garnet-based composite cathodes: the impact of NCM composition on material compatibility, ACS Appl. Energy Mater. 5 (6) (2022) 6913–6926.

[10] X. Yin, D. Li, L. Hao, Y. Wang, Y. Wang, X. Guo, S. Zhao, B. Wang, L. Wu, H. Yu, A high-energy all-solid-state lithium metal battery with "single-crystal" lithium-rich layered oxides, Chem. Commun. 59 (5) (2023) 639–642.

[11] W.S. Scheld, K. Kim, C. Schwab, A.C. Moy, S.K. Jiang, M. Mann, C. Dellen, Y. J. Sohn, S. Lobe, M. Ihrig, M.G. Danner, The riddle of dark LLZO: cobalt diffusion in garnet separators of solid-state lithium batteries, Adv. Funct. Mater. 33 (43) (2023) 2302939.

[12] M.M.U. Din, L. Ladenstein, J. Ring, D. Knez, S. Smetaczek, M. Kubicek, M. Sadeqi-Moqadam, S. Ganschow, E. Salagre, E.G. Michel, S. Lode, A guideline to mitigate interfacial degradation processes in solid-state batteries caused by cross diffusion, Adv. Funct. Mater. 33 (42) (2023) 2303680.

[13] M. Ihrig, L.Y. Kuo, S. Lobe, A.M. Laptev, C.A. Lin, C.H. Tu, R. Ye, P. Kaghazchi, L. Cressa, S. Eswara, S.K. Lin, Thermal recovery of the electrochemically degraded $LiCoO_2/Li_7La_3Zr_2O_{12}$: al, Ta interface in an all-solid-state lithium battery, ACS Appl. Mater. Interfaces 15 (3) (2023) 4101–4112.

[14] K. Touidjine, M. Finsterbusch-Rosen, V. Kiyek, S. Ganapathy, M. Finsterbusch, O. Guillon, M. Huijben, E. Kelder, M. Wagemaker, D. Fattakhova-Rohlfing, The impact of lithium carbonate on tape cast LLZO battery separators: a balanced interplay between lithium loss and relithiation, Energy Storage Mater. 71 (2024) 103487.

[15] R. Ye, C.-L. Tsai, M. Ihrig, S. Sevinc, M. Rosen, E. Dashjav, Y.J. Sohn, E. Figgemeier, M. Finsterbusch, Water-based fabrication of garnet-based solid electrolyte separators for solid-state lithium batteries, Green Chem. 22 (2020) 4952–4961.

[16] M. Rosen, R. Ye, M. Mann, S. Lobe, M. Finsterbusch, O. Guillon, D. Fattakhova-Rohlfing, Controlling the lithium proton exchange of LLZO to enable reproducible processing and performance optimization, J. Mater. Chem. A 9 (8) (2021) 4831–4840.

[17] K.J. Kim, J.L. Rupp, All ceramic cathode composite design and manufacturing towards low interfacial resistance for garnet-based solid-state lithium batteries, Energy Environ. Sci. 13 (12) (2020) 4930–4945.

[18] G.T. Hitz, D.W. McOwen, L. Zhang, Z. Ma, Z. Fu, Y. Wen, Y. Gong, J. Dai, T. R. Hamann, L. Hu, E.D. Wachsman, High-rate lithium cycling in a scalable trilayer li-garnet-electrolyte architecture, Mater. Today 22 (2019) 50–57.

[19] K.J. Kim, M. Balaish, M. Wadaguchi, L. Kong, J.L. Rupp, Solid-state Li–metal batteries: challenges and horizons of oxide and sulfide solid electrolytes and their interfaces, Adv. Energy Mater. 11 (1) (2021) 2002689.

[20] M. Balaish, J.C. Gonzalez-Rosillo, K.J. Kim, Y. Zhu, Z.D. Hood, J.L. Rupp, Processing thin but robust electrolytes for solid-state batteries, Nat. Energy 6 (3) (2021) 227–239.

[21] X. Han, Y. Gong, K. Fu, X. He, G.T. Hitz, J. Dai, A. Pearse, B. Liu, H. Wang, G. Rubloff, Y. Mo, Negating interfacial impedance in garnet-based solid-state Li metal batteries, Nat. Mater. 16 (5) (2017) 572–579.

[22] M. Ihrig, M. Finsterbusch, A.M. Laptev, C.H. Tu, N.T.T. Tran, C.A. Lin, L.Y. Kuo, R. Ye, Y.J. Sohn, P. Kaghazchi, S.K. Lin, Study of $LiCoO_2/Li_7La_3Zr_2O_{12}$: ta interface degradation in all-solid-state lithium batteries, ACS Appl. Mater. Interfaces 14 (9) (2022) 11288–11299.

[23] P. Barai, T. Rojas, B. Narayanan, A.T. Ngo, L.A. Curtiss, V. Srinivasan, Investigation of delamination-induced performance decay at the cathode/LLZO interface, Chem. Mater. 33 (14) (2021) 5527–5541.

[24] J. Liu, H. Yuan, H. Liu, C.Z. Zhao, Y. Lu, X.B. Cheng, J.Q. Huang, Q. Zhang, Unlocking the failure mechanism of solid-state lithium metal batteries, Adv. Energy Mater. 12 (4) (2022) 2100748.

[25] S. Wang, S. Bessette, R. Gauvin, G.P. Demopoulos, 4.8-V all-solid-state garnet-based lithium-metal batteries with stable interface, Cell Rep. Phys. Sci. 5 (10) (2024) 102213.

[26] Y. Xie, L. Huang, Y. Chen, A porous garnet $Li_7La_3Zr_2O_{12}$ scaffold with interfacial modification for enhancing ionic conductivity in PEO-based composite electrolyte, J. Membr. Sci. 683 (2023) 121784.

[27] S.H. Jo, P. Muralidharan, D.K. Kim, Electrical characterization of dense and porous nanocrystalline Gd-doped ceria electrolytes, Solid State Ionics 178 (39–40) (2008) 1990–1997.

[28] H. Zhang, F. Okur, B. Pant, M. Klimpel, S. Butenko, D.T. Karabay, A. Parrilli, A. Neels, Y. Cao, K.V. Kravchyk, M.V. Kovalenko, Garnet-based solid-state Li batteries with high-surface-area porous LLZO membranes, ACS Appl. Mater. Interfaces 16 (10) (2024) 12353–12362.

[29] Ø. Gullbrekken, K. Eggestad, M. Tsoutsouva, B.A. Williamson, D. Rettenwander, M. A. Einarsrud, S.M. Selbach, Phase evolution and thermodynamics of cubic $Li_{6.25}Al_{0.25}La_3Zr_2O_{12}$ studied by high-temperature X-ray diffraction, Inorg. Chem. 64 (12) (2025) 5856–5865.

[30] C. Yang, L. Zhang, B. Liu, S. Xu, T. Hamann, D. McOwen, J. Dai, W. Luo, Y. Gong, E. D. Wachsman, L. Hu, Continuous plating/stripping behavior of solid-state lithium metal anode in a 3D ion-conductive framework, Proc. Natl. Acad. Sci. 115 (15) (2018) 3770–3775.

[31] W. Lu, M. Xue, C. Zhang, Modified $Li_7La_3Zr_2O_{12}$ (LLZO) and LLZO-polymer composites for solid-state lithium batteries, Energy Storage Mater. 39 (2021) 108–129.

[32] M. Kobayashi, Y. Matsumoto, A. Ishida, K. Ute, K. Hatada, Polymorphic structures and molecular vibrations of linear oligomers of polyoxymethylene studied by polarized infrared and Raman spectra measured on single crystals, Spectrochim. Acta Mol. Spectros 50 (8–9) (1994) 1605–1617.

[33] M. Kobayashi, M. Sakashita, M. Hasegawa, Infrared and Raman spectra of macrocyclic poly (oxymethylene), Macromolecules 24 (17) (1991) 4796–4800.

[34] Z. Li, R. Yu, S. Weng, Q. Zhang, X. Wang, X. Guo, Tailoring polymer electrolyte for high-voltage solid-state Li metal batteries working at ultra-low temperatures. https://doi.org/10.21203/rs.3.rs-1771051/v1, 2022.

[35] J.L. Allen, S.D. Han, P.D. Boyle, W.A. Henderson, Crystal structure and physical properties of lithium difluoro (oxalato) borate (LiDFOB or $LiBF_2O_x$), J. Power Sources 196 (22) (2011) 9737–9742.

[36] J. Li, P. Meng, H. Zhou, Regularities of ionic solvation and association of lithium difluoro (oxalate) borate in dimethyl carbonate and sulfolane solvent systems, Ionics 24 (7) (2018) 2147–2155.

[37] V. Vanita, A.I. Waidha, S. Yadav, J.J. Schneider, O. Clemens, Conductivity enhancement within garnet-rich polymer composite electrolytes via the addition of succinonitrile, Int. J. Appl. Ceram. Technol. 20 (1) (2023) 236–250.

[38] S. Wang, G.P. Demopoulos, High-conductive polymer-in-porous garnet solid electrolyte structure for all-solid-state lithium batteries enabled by molecular engineering, Energy Storage Mater. 71 (2024) 103604.

[39] Q. Chen, C. Ouyang, Y. Liang, H. Liu, H. Duan, Composite polymer electrolyte with vertically aligned garnet scaffolds for quasi solid-state lithium batteries, Energy Storage Mater. 69 (2024) 103418.

[40] H. Zhang, R. Dubey, M. Inniger, F. Okur, R. Wullich, A. Parrilli, D.T. Karabay, A. Neels, K.V. Kravchyk, M.V. Kovalenko, Ultrafast-sintered self-standing LLZO membranes for high energy density lithium-garnet solid-state batteries, Cell Rep. Phys. Sci. 4 (7) (2023) 101473.

[41] D. Cai, D. Wang, Y. Chen, S. Zhang, X. Wang, X. Xia, J. Tu, A highly ion-conductive three-dimensional LLZAO-PEO/LiTFSI solid electrolyte for high-performance solid-state batteries, Chem. Eng. J. 394 (2020) 124993.

[42] X. Liu, Z. Xiao, H. Peng, D. Jiang, H. Xie, Y. Sun, S. Zhong, Z. Qian, R. Wang, Rational design of LLZO/polymer solid electrolytes for solid-state batteries, Chem.–Asian J. 17 (24) (2022) e202200929.

[43] R. Grissa, L. Seidl, W. Dachraoui, U. Sauter, C. Battaglia, $Li_7La_3Zr_2O_{12}$ protonation as a means to generate porous/dense/porous-structured electrolytes for all-solid-state lithium-metal batteries, ACS Appl. Mater. Interfaces 14 (40) (2022) 46001–46009.

[44] H. Noh, D. Kim, W. Lee, B. Jang, J.S. Ha, J.H. Yu, Surface modification of Ga-Doped-LLZO ($Li_7La_3Zr_2O_{12}$) by the addition of polyacrylonitrile for the electrochemical stability of composite solid electrolytes, Energies 16 (23) (2023) 7695.

[45] a C.L. Tsai, V. Roddatis, C.V. Chandran, Q. Ma, S. Uhlenbruck, M. Bram, P. and Heitjans, O. Guillon, ACS Appl. Mater. Interfaces 8 (2017) 10617–10626, 2016.d)W. Wachsman, L. Hu, Adv. Mater., 29, p.1606042.